JACS
JOURNAL OF THE AMERICAN CHEMICAL SOCIETY
Article
pubs.acs.org/JACS

Rational Design of Monocrystalline $(InP)_yGe_{5-2y}$/Ge/Si(100) Semiconductors: Synthesis and Optical Properties

Patrick E. Sims,[†] Andrew V.G. Chizmeshya,*[,†] Liying Jiang,[‡] Richard T. Beeler,[†] Christian D. Poweleit,[‡] James Gallagher,[‡] David J. Smith,[‡] José Menéndez,[‡] and John Kouvetakis[†]

[†]Department of Chemistry and Biochemistry, Arizona State University, Tempe, Arizona 85287-1604, United States
[‡]Department of Physics, Arizona State University, Tempe, Arizona 85287-1504, United States

ABSTRACT: In this work, we extend our strategy previously developed to synthesize functional, crystalline $Si_{5-2y}(AlX)_y$ {X = N,P,As} semiconductors to a new class of Ge−III−V hybrid compounds, leading to the creation of $(InP)_yGe_{5-2y}$ analogues. The compounds are grown directly on Ge-buffered Si(100) substrates using gas source MBE by tuning the interaction between Ge-based $P(GeH_3)_3$ precursors and In atoms to yield nanoscale "In−P−Ge_3" building blocks, which then confer their molecular structure and composition to form the target solids via complete elimination of H_2. The collateral production of reactive germylene (GeH_2), via partial decomposition of $P(GeH_3)_3$, is achieved by simple adjustment of the deposition conditions, leading to controlled Ge enrichment of the solid product relative to the stoichiometric $InPGe_3$ composition. High resolution XRD, XTEM, EDX, and RBS indicate that the resultant monocrystalline $(InP)_yGe_{5-2y}$ alloys with y = 0.3−0.7 are tetragonally strained and fully coherent with the substrate and possess a cubic diamond-like structure. Molecular and solid-state ab initio density functional theory (DFT) simulations support the viability of "In−P−Ge_3" building-block assembly of the proposed crystal structures, which consist of a Ge parent crystal in which the P atoms form a third-nearest-neighbor sublattice and "In−P" dimers are oriented to exclude energetically unfavorable In−In bonding. The observed InP concentration dependence of the lattice constant is closely reproduced by DFT simulation of these model structures. Raman spectroscopy and ellipsometry are also consistent with the "In−P−Ge_3" building-block interpretation of the crystal structure, while the observation of photoluminescence suggests that $(InP)_yGe_{5-2y}$ may have important optoelectronic applications.

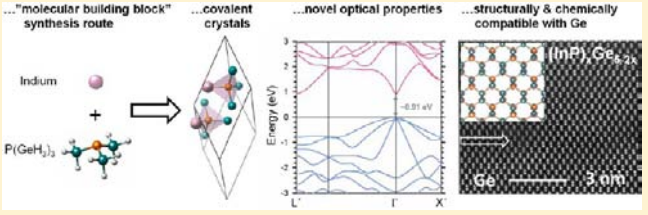

INTRODUCTION

The active materials in most electronic devices are either elemental semiconductors from group IV of the periodic table or compounds based on one element from group III and one element from group V. Alloys combining elements within each class of materials are well-known scientifically and very important in technology. On the other hand, interclass alloys of group IV and III−V materials are expected to have unique properties and applications, but so far the dearth of general synthetic methodologies for the construction of single phase materials has prevented their widespread use and made the research of their properties very difficult.[1−6]

Very recently, we have introduced new synthetic pathways of the above interclass tetrahedral semiconductors consisting of III−V donor−acceptor dimers incorporated intact within a host Si lattice. Our strategy suppresses phase segregation effects that until now prevented the development of materials in the general class of group III−V and IV hybrids for optoelectronics applications. The crystal growth was conducted using gas-phase reactions of Al atoms with the $N(SiH_3)_3$, $P(SiH_3)_3$, and $As(SiH_3)_3$ molecules. We proposed that these form corresponding Al:$N(SiH_3)_3$, Al:$P(SiH_3)_3$, and Al:$As(SiH_3)_3$ intermediate complexes which in turn eliminate the H_2 to yield preformed Al:NSi_3, Al:PSi_3, and Al:$AsSi_3$ tetrahedral cores. These are then self-assembled into single-phase monocrystalline epilayers via epitaxy-driven mechanisms in a manner that precludes the formation of thermodynamically unfavorable Al−Al bonds. To date, this approach has been used to grow new compounds such as $AlPSi_3$ and $AlAsSi_3$, as well as corresponding alloys $Al(As_{1-x}P_x)Si_3$, $Al(As_{1-x}N_x)Si_3$, and $Al(P_{1-x}N_x)Si_3$. More generally, we have shown that an even broader range of compositions $Al(As,P,N)_ySi_{5-2y}$ is accessible, spanning stoichiometric phases (y = 1) which represent the maximum concentration (40%) of isolated III−V pairs to highly diluted system approaching the Si limit ($y \rightarrow 0$).[7−11] This work has generated growing interest from both theoretical and experimental perspectives because these materials have been predicted to exhibit unique absorption properties in a wavelength range needed for dramatic efficiency gains for the next generation of Si-based photovoltaics.[12,13]

In this paper, we demonstrate the generality of this building-block approach by using reactions of In atoms and $P(GeH_3)_3$, the Ge molecular analogue of the above precursors, to synthesize $(InP)_yGe_{5-2y}$ tetrahedral semiconductors for the first time. As in the case of the silicon systems above, these materials are composed of isolated InP donor−acceptor dimers substituted within a diamond-cubic Ge parent lattice. In

Received: June 13, 2013
Published: July 30, 2013

   dx.doi.org/10.1021/ja405726b | J. Am. Chem. Soc. 2013, 135, 12388−12399

particular, InP was selected because it represents a well-known binary semiconductor widely used in modern photonics. Furthermore, from a synthesis perspective, the $P(GeH_3)_3$ precursor has been shown theoretically to combine favorably with In atoms to form the hypothetical $In:P(GeH_3)_3$ intermediated complexes en route to the desired $In:PGe_3$ building blocks. We anticipate that these Ge-based materials may have applications in various fields of optoelectronics, including direct-gap laser materials and semiconductors with widely tunable infrared band gaps. From a fundamental perspective, our alloying strategy represents a viable approach to extending the basic properties and optical capabilities of Ge by controlling the crystalline composition at the nanoscale via substitution of Ge−Ge bonds by In−P pairs. As we show below, the alloying maintains the molar volume close to that of Ge, allowing facile integration on Ge-based platforms. The recent advent of commercial quality Ge-buffered Si wafers introduces intriguing opportunities for this system in the area of heteroepitaxial photonic applications straddling the properties of the ubiquitous InP and Ge end-systems.

Our work utilizes the above platforms to fabricate new series of monocrystalline $(InP)_yGe_{5-2y}$ alloys with y = 0.70−0.30 corresponding to molar concentrations of InP between 30 and 10%. Structural characterization shows that materials across the entire concentration range exhibit tunable lattice constants that closely follow Vegard's linear interpolation between the InP and Ge end-members. Initial spectroscopic ellipsometry studies indicate that InP-rich alloys approaching the stoichiometric limit exhibit dielectric properties distinct from those of pure InP or Ge while the Ge-rich counterparts possess Ge-like transition energies. Photoluminescence (PL) studies suggest that this approach may enable compositional tuning of direct gaps below that of Ge (0.80 eV) in the near-infrared. Raman scattering contradicts the possibility of phase separation but supports the existence of isolated "In−P" dimers within a crystalline Ge host matrix. The latter bonding motif is corroborated by density functional theory simulations at both the molecular and solid-state level which reproduce the observed compositional dependence of the lattice constants and provide direct support for the notion that the $(InP)_yGe_{5-2y}$ materials can be formed via assembly of $In-P-Ge_3$ building blocks over the full range of compositions explored.

EXPERIMENTAL SECTION

The $(InP)_yGe_{5-2y}$ films were grown on Ge-buffered Si wafers by gas-source molecular beam epitaxy (GS MBE) at 450−300 °C. The Ge buffers were grown on 4 in. p-type Si(100) with 1−10 Ω cm resisitivity via previously developed deposition protocols using a pure tetragermane source. This technique produces highly aligned monocrystalline films with atomically flat surfaces devoid of defects as required for subsequent use as templates. The as-grown Ge/Si(100) wafers were cleaved to 1 × 1.5 cm^2 size substrate segments that fit the dimensions of the sample stage. Each substrate was sonicated in 10% HF/methanol and pure methanol baths for 5 min each, dried under a stream of nitrogen, and inserted into the chamber via a load-lock at 3 × 10^{-10} Torr. The substrate was then heated at 600 °C under vacuum to remove residual impurities from the surface. Prior to growth, the temperature of the wafer was adjusted to the desired setting using a single-color pyrometer. The crystal nucleation was initiated by first introducing the In atoms generated by a Knudsen cell into the growth chamber. The gaseous $P(GeH_3)_3$ source was then admitted through a nozzle 2−3 cm away from the substrate holder. After a brief period of equilibration in the reaction zone, the sample stage was rotated to expose the growth surface to the combined incoming flux of the reactants and commence the film growth process. The gas flow was subsequently controlled by a needle valve at a steady rate giving a nominal 1:1 molar ratio with the In atoms. The evaporation rate of the latter was regulated by the temperature of the Knudsen cell. The reaction pressure was maintained constant at ∼8 × 10^{-6} Torr via dynamic pumping using a turbo pump. The typical deposition time frame was 30−60 min to produce films with thicknesses in the range of 350−1250 nm at growth rates between 17 and 22 nm/min depending on temperature.

RESULTS AND DISCUSSION

Previously, we have shown that $P(GeH_3)_3$ reacts readily at temperatures as high as 430 °C via complete elimination of H_2 to produce device quality n-type Ge layers doped with P atoms.[14] Under these conditions, the compound delivers the entire PGe_3 molecular core which incorporates intact into the crystal leading to the formation of atomically flat monocrystalline semiconductor layers. In this work, we find that reactions of $P(GeH_3)_3$ and In atoms yield uniform and crystalline $(InP)_yGe_{5-2y}$ layers only within a narrow operating temperature range from 430 to 330 °C, in which the upper limit coincides with the one determined in the doping studies of the $P(GeH_3)_3$ source. Within the optimal window, the concentration of InP varies from 10% at 430 °C to 30% at 330 °C, never reaching the 40% stoichiometric limit corresponding to $InPGe_3$. We note that this trend follows the one observed in the $(AlP)_ySi_{5-2y}$ systems.[8] However, the stoichiometric $AlPSi_3$ (40% AlP) was attained at the lower temperature range in those experiments. Above the viable 430−330 °C growth window, the highly reactive $P(GeH_3)_3$ rapidly dissociates to form PH_3, precluding the reaction with indium to form the desired gas phase $In:P(GeH_3)_3$ entities and ultimately yielding rough samples through segregation of elemental In and Ge precipitates. Attempts to lower the reaction temperature below 330 °C also yielded poor noncrystalline products akin to those found for T > 430 °C. In this case, the activation barrier to form and/or dehydrogenate the intermediate $In:P(GeH_3)_3$ complex may be too high to allow assembly of crystalline materials based on $InPGe_3$ cores. Accordingly, under the latter growth conditions, the observed film stoichiometries straddle 30% (i.e., $InPGe_{4.5-5}$) but never reach the 40% limiting value (i.e., $InPGe_3$) as indicated above.

The proposed growth pathway is consistent with control experiments of single-source $P(GeH_3)_3$ depositions (in the absence of In) over the same optimal growth window, which yield substantial Ge film growth on the buffer layer surface. Accordingly, the depletion of (In, P) with increasing temperature in our alloys can be explained by the facile decomposition of $P(GeH_3)_3$ as described by a chain of thermally activated side reaction:

$$P(GeH_3)_3 \rightarrow PH(GeH_3)_2 + GeH_2 \rightarrow PH_3 + 3GeH_2 \quad (1)$$

In this scenario, volatile byproducts of the $PH_x(GeH_3)_{3-x}$ (x = 1−3) variety are eliminated. These do not react with In atoms and are thus pumped away, while the highly reactive GeH_2 (germylene) species remain on the surface and incorporate into the crystal as Ge atoms. The net result is a Ge-enriched lattice comprised of tetrahedral $InPGe_3$ units interlinked with Ge atoms.

On the basis of the above synthesis strategy, a series of alloys were grown and characterized. The film morphology was examined by Nomarski imaging, revealing a typically smooth surface with no cracks or other imperfections visible throughout the wafer surface. This was corroborated by AFM measure-

ments, which gave relatively low RMS roughness of ~1.5−2 nm from 20 μm × 20 μm areas. The sample stoichiometry, thicknesses, and crystallinity were determined by Rutherford backscattering spectrometry (RBS). Random spectra acquired at 2 and 3.7 MeV showed distinct signals corresponding to In, Ge, and P (see Figure 1). The 3.7 MeV measurements were

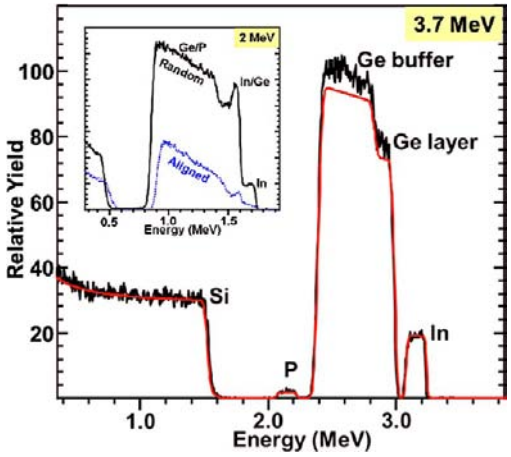

Figure 1. 3.7 MeV RBS spectra of In/P/Ge film grown on Ge/Si(100) showing distinct signals of the elements in the epilayer and Ge buffer. Quantitative modeling of the random trace (red line) yields an average composition of $InPGe_6$ (black line) and a thickness of 200 nm. Inset: 2 MeV spectra of the same sample showing a high degree of channeling consistent with the full substitutionallity of the three elements in the cubic alloy structure.

used to clearly separate Ge peaks from the film and the buffer in samples thicker than ~200 nm, thereby allowing precise quantification of the chemical composition. The films grown at 330 °C typically exhibited a nominal RBS stoichiometry of $InPGe_{4.5-5}$ (here we use the more compact notation $InPGe_{(5-2y)/y}$ instead of the standard $(InP)_yGe_{5-2y}$, which can also be described as 30% InP and 70% Ge. The films produced between 330 and 430 °C contained a Ge fraction spanning the 70 −90% range. In all cases, the In:P ratio was found to be 1:1 (30−10% InP), suggesting that these Ge-rich systems are likely formed by replacing Ge−Ge dimers in the parent structure by In−P pairs. RBS channeling indicated monocrystalline and highly aligned materials. The ratio of the aligned versus random peak heights (χ_{min}) of the In, Ge, and P signals was observed to rapidly decrease across the film thickness toward the interface, indicating a high degree of epitaxial commensuration in all samples. Furthermore, the χ_{min} values for In, Ge, and P were found to be nearly the same in any given sample, indicating complete substitution of the atoms in the same structure.

The RBS analysis indicated that the Ge-rich layers produced at the higher temperatures typically exhibited a large thickness on the order of 0.8−1.2 μm owing to higher growth rates afforded by the increased thermal activation of the reactants. The lattice dimensions and strain properties of these materials were measured by high-resolution X-ray diffraction (HR-XRD). In general, the XRD analyses show that the layers are compressively strained as a result of the mismatch between the alloy and the Ge template. We note that the latter exhibit a slight tensile strain induced by heating the wafers to 600 °C to desorb the surface oxide and then quenching to room temperature prior to growth yielding $a = b = 5.668$ Å and $c = 5.649$ Å. This tetragonal deformation fortuitously offers an advantage over bulk Ge because the slight increase in the in-plane lattice parameter allows better lattice matching of the epilayers with the target alloys.

The $\theta/2\theta$ scans of the Ge-rich epilayers typically revealed a strong but asymmetric peak with angular position clearly distinct from that of either InP or elemental Ge. The origin of the asymmetry is a result of a shoulder peak at lower diffraction angle with d-spacing very close to that of the main reflection. The off-axis (224) reciprocal space maps revealed two closely spaced broad peaks with asymmetrical shapes that extend to the right of the pseudomorphic line toward higher reciprocal Q_x values or a smaller d-spacing (see Figure 2). These two peaks

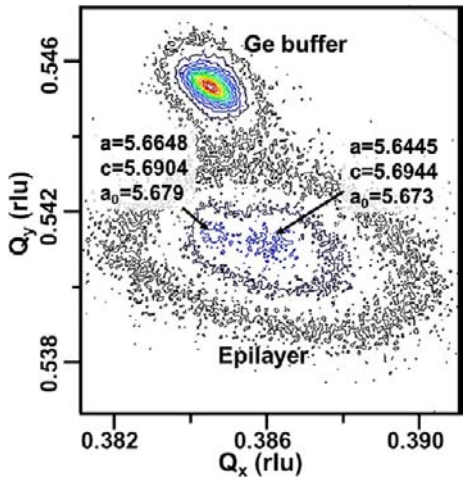

Figure 2. XRD (224) reciprocal space maps of $InPGe_{15}$/Ge/Si(100) showing separate peaks for the fully strained bottom and over relaxed top sections of the film. In both cases, the plots yield very similar values for the relaxed lattice constants (a_0), indicating no significant change in molar volume across the sample.

correspond, respectively, to a fully strained bottom and an over-relaxed top of the $(InP)_yGe_{5-2y}$ layer. The (224) and (004) XRD plots were analyzed to determine in plane (a) and vertical (c) parameters for the two regions, indicating that the alloy layer in this case is gradually over-relaxing relative to the Ge buffer.

As an example, the (224) ($\phi = 0°$) plots of an $InPGe_{15}$ layer with thickness of 900 nm showed a double peak structure yielding in-plane lattice parameters $a_1 = 5.6648$ Å and $a_2 = 5.644$ Å. The first corresponds to a fully strained layer adjacent to the interface, while the other is slightly smaller consistent the over-relaxation in the upper segment of the layer. The corresponding vertical lattice constants are smaller ($c_1 = 5.6904$) near the interface and larger ($c_2 = 5.6944$ Å) in the over-relaxed region of the film. Collectively, the data indicate that the molar volume is essentially preserved across the film as evidenced by the nearly equal values of the relaxed lattice parameters $a_{01} = 5.679$ Å and $a_{02} = 5.673$ Å. The latter are calculated by linearly interpolating the C_{12}/C_{11} elastic constant ratios of Ge and InP and are found to be close to the Vegard's law average of 5.683 Å determined using $a_{InP} = 5.8687$ Å and $a_{Ge} = 5.658$ Å. To exclude lower symmetry orthorhombic deviations in the over-relaxed samples, we also measured the $(\bar{2}24)$ ($\phi = 90°$) reciprocal space maps. The diffraction plots in this case were found to be virtually identical for both (224) and $(\bar{2}24)$ maps each showing two peaks with matching reciprocal point values yielding in-plane lattice constants within the error

dx.doi.org/10.1021/ja405726b | J. Am. Chem. Soc. 2013, 135, 12388−12399

of the measurement ($\Delta a/a \sim 0.02\%$). Finally, we note that similar observations of tetragonal over-relaxation of misfit strain has been previously found in heavily carbon doped GaAs films and are attributed to the formation of unusual defect structures.[15]

For samples grown at lower temperatures in which the InP concentration is increased from ~20 to 30% ($InPGe_9$ to $InPGe_{4.5}$), the diffraction data show sharper and more intense asymmetrical (004) peaks due to improved crystallinity (see Figure 3 for typical diffraction patterns). In all cases, the (224)

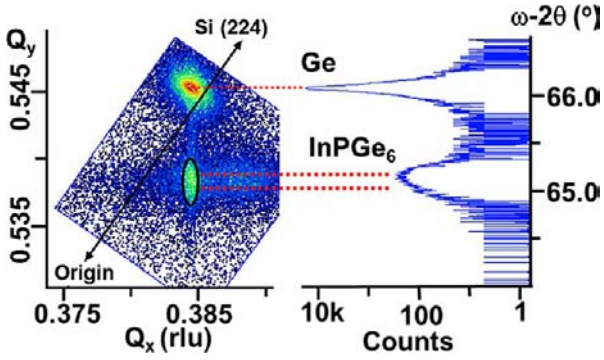

Figure 3. XRD plots of $InPGe_6$/Ge/Si(100) sample. (left) Reciprocal space maps in the vicinity of the (224) reflection of the cubic structure showing in-plane lattice matching between the compressively strained epilayer and the tensile strained buffer. Note that the Ge peak maximum lies above the relaxation line (double arrow) as expected. (right) Corresponding 004 2-θ plots of the heterostructure showing a slightly asymmetric and broad alloy peak relative to that of the Ge buffer. The XRD data confirm the high crystalline quality of the epilayer.

RSM analogues exhibit a corresponding sharp and highly intense diffraction map that is elongated in the vertical direction and exactly aligned with the Ge buffer peak along the pseudomorphic line, indicating perfect in-plane lattice-matching between the two materials. Figure 3 shows XRD plots for a representative $InPGe_{6.3}$ film with thickness of 350 nm. The (004) reflection contains a strong main peak and a lower intensity shoulder, yielding c = 5.7211 Å and c = 5.7280 Å, respectively. As shown by the dotted lines, the (224) counterparts overlap in the vertical direction (same Q_x values), yielding a common in plane lattice constant a = 5.668 Å which is identical to that of the underlying Ge, indicating that the epilayer is pseudomorphic. The calculated a_0 values in this sample are 5.702 Å and 5.698 Å, which are both close to the Vegard'a law value a_{Vegard} = 5.709 Å. We attribute the slightly different (c) lattice dimensions to small variations in alloy concentration as discussed below. It is worth noting that the over-relaxation behavior appears to be a strong function of thickness and not composition. For a range of samples with different Ge compositions, layer over-relaxation is not observed in thinner films because they are within range of their critical thicknesses. A Ge-rich $InPGe_9$ film with thickness of 1200 nm shows over-relaxation throughout a significant portion of the layer, while the effect appears to be absent in a 300 nm analogue grown with virtually identical composition.

As shown in Figure 3, in addition to sharp (224) diffraction spots, we also observe in most samples a broad, diffuse background whose maximum intensity is significantly weaker but above the noise level relative to the primary peak. The center of this feature exhibits a slightly smaller (220) d-spacing than that of the main peak, indicating a correspondingly reduced (a) parameter, by an average 0.04 Å in thinner samples. With increasing sample thickness from 100 to 600 nm, this features significantly increases in intensity and systematically coalesces with the pseudomorphic peak. In these cases, the (004) counterpart shows a similar Q_y value for both peaks, implying a slightly reduced (1−1.5%) molar volume of any material associated with this broad scattering. This observation is difficult to reconcile with measurable variations in composition. However, the increase of intensity of the secondary diffuse peak is consistent with scattering from misalignment or over-relaxations of columns in the upper portion of the layer, leading to defects localized near the free surface. Ultimately, the coalescence of the (224) peaks with increasing thickness culminates in diffractions maps of the type described for the over-relaxed structures in Figure 2 for 900 nm thick samples where two closely spaced broad peaks with asymmetrical shapes in essence virtually coincide. Another possibility consistent with the absence of compositional changes is the existence of a strain-induced polymorphic structure with reduced molar volume, for which a tetragonal distortion is stabilized.

Further structural analysis was conducted using cross-sectional transmission electron microscopy (XTEM), which demonstrated the presence of smooth, uniform, and crystalline layers exhibiting comparable thicknesses to those estimated by RBS. Figure 4 is a representative Z-contrast image of the most

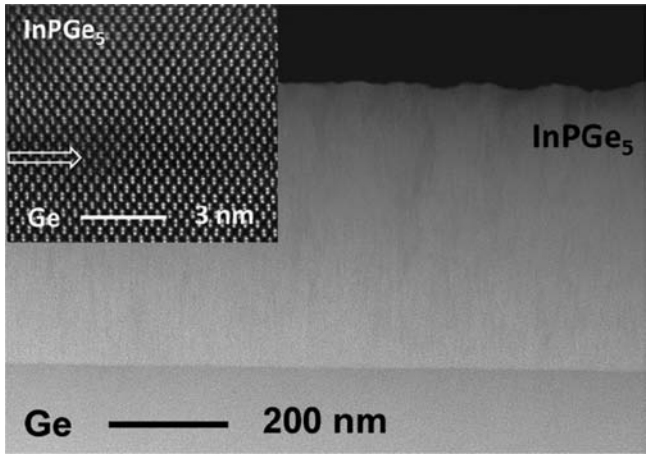

Figure 4. Z-Contrast XTEM micrograph of $InPGe_5$ film (brighter contrast) grown on Ge buffer with thickness of ~500 nm showing columnar features and vertical striations particularly near the top thinner portion of the layer. Inset: Z-Contrast high resolution image from interface region between film and Ge buffer showing high quality epitaxy and sharp Ge−$InPGe_5$ heterojunction marked by arrow.

commonly found microstructure showing a sharp and uniform interface between the slightly brighter region alloy and the Ge buffer. High-resolution images (inset) from the interface region taken in (110) projection exhibit elongated bright spots corresponding to pairs of In/P/Ge atoms or "dumbbells". The XTEM micrographs of these samples also reveal highly oriented columnar features that appear to extend downward from the surface through a significant portion of the layer. Toward the surface where the sample is thinner, the film clearly exhibits a nearly periodic pattern of parallel striations aligned along the growth axis. These are likely associated with slight inhomogeneities of the alloy composition induced by

dx.doi.org/10.1021/ja405726b | J. Am. Chem. Soc. 2013, 135, 12388−12399

fluctuation in growth conditions including temperature, pressure, and possibly precursor flux, all of which may have a significant effect on the instantaneous growth rate. This observation is not unexpected because both the complexity of the reaction mechanism and the crystal assembly at ultralow temperatures employed here (>350 °C) are both exceedingly sensitive to such fluctuations.

To further investigate possible compositional variations, we conducted atomic-level EDX analysis with a 1.5 Å electron probe to study the uniformity of elemental distribution at the nanoscale. Typical elemental profiles were scanned both horizontally across columns and vertically within a given column in the film. In both cases, all three constituent elements, In, P, and Ge, appeared in every atomic-scale region probed, without any indication of phase separation of InP and Ge or any segregation of individual elements. The atomic resolution analysis results thus confirm that the film contains an alloy of Ge and In−P at the atomic scale. Figure 5 shows a representative high resolution micrograph in [110] projection clearly showing continuous (111) lattice planes of the cubic structure spanning a field of view containing a column (bright region) and its adjacent boundary (dark vertical band), with no visible discontinuity or local defects of the crystal lattice across both regions. The horizontal EDX line scans show that the elemental profiles are uniform across the column whose average RBS composition is determined to be close to $InPGe_5$. However, within the narrow boundary region, the corresponding Ge/InP EDX counts show a sharp decrease/increase representing compositional variations of the type discussed above. In this example, the changes in Ge and In−P content are estimated to correspond to $InPGe_{4-3.5}$, which is closer to the target stoichiometric $InPGe_3$ limit.

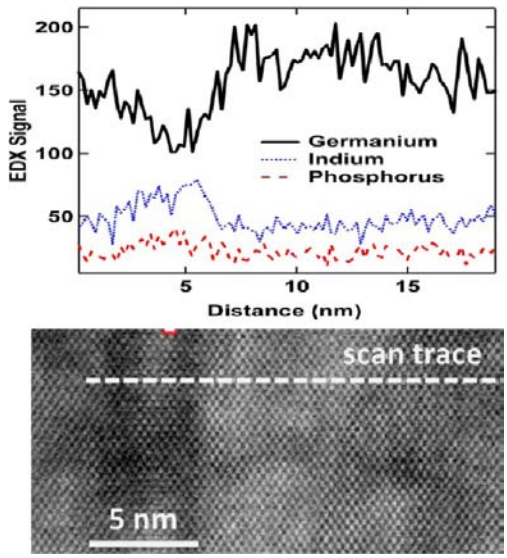

Figure 5. (top) EDX elemental profile scan of Ge (black line), In (blue line), and P (red line) sampled across 20 nm over a film with average $InPGe_5$ RBS composition, showing the distribution of all three constituent elements. (bottom) Bright field high-resolution micrograph shows the region where the analysis took place on the film at the edge of a column and its boundary (darker intensity band at right). The scan is marked by a white dotted line in the upper portion of the image.

The above analysis is consistent with the XRD data for this sample, which also showed a main (004) peak and a shoulder in analogy with the alloy described in Figure 3. The latter peak gives a slightly larger lattice constant corresponding to InP-rich material of the type observed at the boundary of columns in the TEM images. The calculated relaxed lattice constants for the bulk material and the more concentrated narrow bands are 5.703 and 5.707 Å, which on the basis of Vegard's Law correspond to $InPGe_5$ and $InPGe_4$, respectively. This is consistent with the estimates provided by the nanoanalysis results in Figure 5. We note that this compositional change corresponds to an increase in molar volume and cannot be associated with the diffuse peak discussed earlier, which in this case has almost coalesced with the main peak in the XRD spectra.

Next we conducted optical characterization of the alloys using spectroscopic ellipsometry (SE), photoluminescence (PL), and Raman scattering to investigate their dielectric function, direct gap emission, and local bonding properties. Figure 6 shows the complex pseudodielectric function for the $InPGe_5$ sample in Figures 4 and 5 and for the $InPGe_{15}$ sample in Figure 2, measured using a variable-angle spectroscopic ellipsometer (VASE from J.A. Woollam Co.) with a computer-controlled compensator. The results were compared with the dielectric function of bulk Ge to highlight the qualitative similarities with the Si-based III−V−IV_3 systems, for which the dielectric function has a line shape similar to a broadened Si dielectric function. In the $(InP)_yGe_{5-2y}$ case, the data in Figure 6 appear as a broadened Ge dielectric function. Whereas the

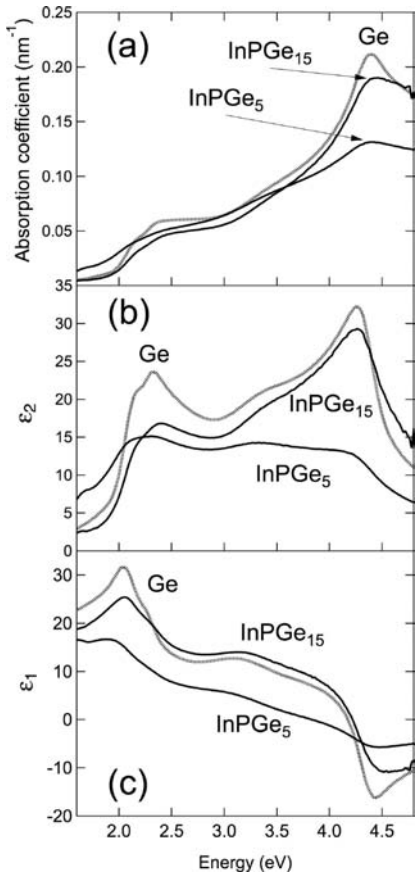

Figure 6. (a) Absorption coefficients calculated from ε_1 and ε_2. (b) Imaginary (ε_2) and (c) real (ε_1) parts of the pseudodielectric function of two $(InP)_yGe_{5-2y}$ films (solid black lines) compared with the dielectric function of bulk Ge (gray line).

dx.doi.org/10.1021/ja405726b | J. Am. Chem. Soc. 2013, 135, 12388−12399

broadening is small for $InPGe_{15}$, as expected, it is substantial for $InPGe_5$. In the latter sample, we also see clear evidence of a downshift in the so-called $E_1/E_1 + \Delta_1$ structure in the 2.0−2.5 eV range. The $E_1/E_1 + \Delta_1$ transitions in InP appear at substantially higher energies than in Ge (ref 16), so that the downshift we observe implies a large quadratic term with a coefficient (bowing parameter) close to $b = 2$ eV. Such large bowing coefficients are in qualitative agreement with findings III−V−Si systems.[11,17] When the linear interpolation is applied to the lowest direct (Γ point in the diamond Brillouin zone) and indirect (L-point) gaps, we predict that the material becomes a direct gap semiconductor for $x > 0.5$, as seen in Figure 7. The predicted band gap value at the indirect-to-direct

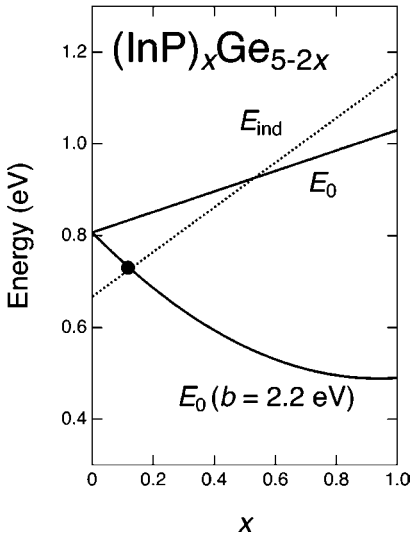

Figure 7. Straight lines show linear interpolations between the direct (solid line) and indirect (dotted line) band gaps of Ge and InP, with data from refs 16, 20, and 21, as discussed in the text. The circular dot shows the measured energy of the PL peak in sample $InPGe_{15}$, and the solid curved line is a calculation of the direct gap of the alloy with a bowing parameter of $b = 2.2$ eV.

transition is $E_0 \sim 0.9$ eV. To shed some light on the possibility of direct gap $(InP)_yGe_{5-2y}$ alloys, we performed preliminary PL experiments. The samples were excited with 400 mW from a 980 nm laser, and the emitted light was analyzed with a Horiba Micro-HR spectrometer equipped with an extended InGaAs detector. Figure 8 shows results for the $InPGe_{15}$ sample. We observe a clear peak near 1700 nm (0.73 eV) mounted on a

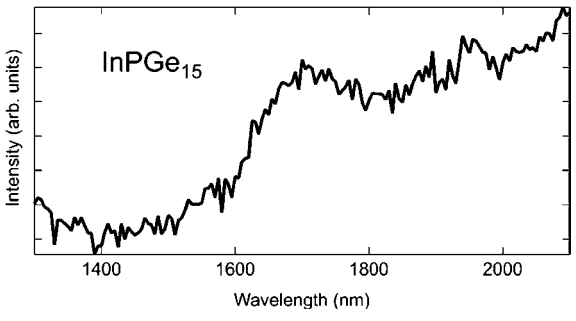

Figure 8. Room temperature photoluminescence of an $InPGe_{15}$ film obtained with 980 nm excitation. The peak near 1700 nm is tentatively assigned to the direct gap E_0 based on similar studies of Ge films. The rising background is probably due to dislocation luminescence.

sloping background, which may be associated with defects.[18] For the $InPGe_5$ sample (not shown), we see a rising PL intensity as we approach the detector cutoff wavelength, suggesting a PL peak below 0.6 eV.

The PL peak energy for the $InPGe_{15}$ sample is shown as a dot in Figure 7, and we see that it is in good agreement with the predicted indirect gap for this composition. However, this agreement may be fortuitous. First, there is no universal agreement as to the exact value of the lowest indirect gap in InP.[19] We use the value obtained in an empirical pseudopotential calculation of the band structure of InP.[20] Because the temperature dependence of this transition is not well-known either, we obtained room temperature values by assuming that the temperature dependence of the direct and indirect edges is the same and using the measured temperature dependence of the E_0 transition.[16] This gives $E_L = 1.88$ eV at room temperature. More importantly, the assignment of the PL peak to the indirect transition would imply that the bowing of the lowest direct and indirect gaps is very small, which appears unlikely. In fact, a bowing parameter $b = 2.2$ eV, very similar to the observed bowing for the $E_1/E_1 + \Delta_1$ manifold, would bring the direct gap energy in agreement with the experimental data point, as seen in Figure 7. Moreover, such a large bowing parameter would imply a lower direct band gap for the $InPGe_5$ sample, as appears to be the case experimentally. Therefore, it is not possible at this time to unambiguously assign the PL peak in Figure 8. Substantial additional work, both experimental and theoretical, will be needed to elucidate the nature of the lowest band gap in these systems, but the results and theoretical analysis do suggest that $(InP)_yGe_{5-2y}$ may be a direct-gap semiconductor over a broad range of compositions. On the experimental side, the role of compositional fluctuations such as those suggested by Figure 5 must be carefully analyzed, particularly in regard to the PL experiments. On the theoretical side, we show below density functional theory calculations within the local density approximation which suggest a direct band gap for $x = 1$, but more accurate band structure methods are required to make reliable predictions.

Figure 9 compares the Raman spectrum of two $Ge_{5-2y}(InP)_y$ samples with that of pure Ge, obtained with 364 nm excitation. At this wavelength, the penetration depth of the light is very small and the signal can be assigned to the top film only. The

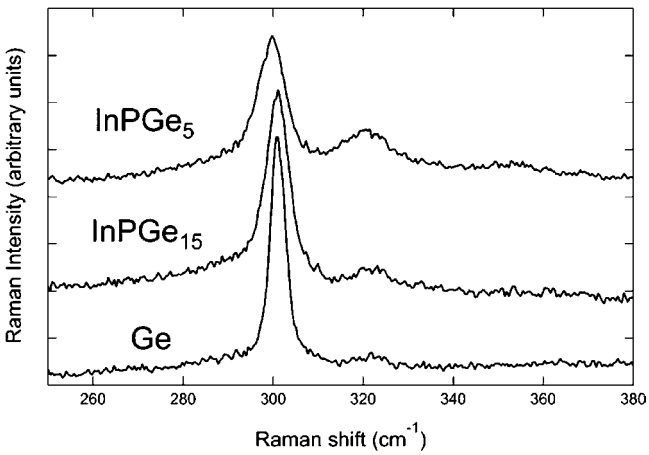

Figure 9. Unpolarized, room temperature Raman spectrum of two $(InP)_yGe_{5-2y}$ samples compared with the Raman spectrum of bulk Ge obtained under the same experimental conditions.

dx.doi.org/10.1021/ja405726b | J. Am. Chem. Soc. 2013, 135, 12388−12399

main Raman peak in the alloy samples is attributed to Ge−Ge vibrations, as it is clearly derived from the Ge Raman peak. The alloy peak is somewhat asymmetric, as observed in other alloy systems, and significantly broadened (by a factor larger than 2) with respect to the Ge reference. At the highest InP concentration, we observe a clear downshift of 0.9 cm^{-1}. These results provide strong evidence of single-phase material precluding phase separation. Whereas the presence of InP pairs uniformly distributed over the Ge matrix accounts for the observed broadening and downshift, similar results can only be observed in pure Ge for particle sizes of about 10 nm.[22] However, the presence of such small crystallites is clearly inconsistent with the single-crystal nature of our films as evidenced by the electron microscopy and X-ray diffraction studies. Moreover, we do not observe the pure InP TO and LO Raman modes at 304 and 345 cm^{-1}, respectively.[23] A relatively narrow second peak is seen near 320 cm^{-1}, and in the $InPGe_5$ sample there is a hint of a third feature emerging near 355 cm^{-1}. The intensity of the 320 cm^{-1} peak appears to scale with the InP concentration, and it is tempting to assign it to vibrations involving the InP bonds in $(InP)_yGe_{5-2y}$. If we subtract the shifts induced by the long-range Coulomb interaction (LO−TO splitting) in bulk InP, we obtain an optical mode frequency of 318 cm^{-1}. Because the LO phonon branches in InP are extremely flat,[24] the highest vibrational mode of an isolated InP pair (involving mainly P-atom displacements) should remain close to 318 cm^{-1}. From this perspective, the observed mode frequency in the 319−322 cm^{-1} range, as seen in Figure 9, appears as reasonable, particularly if we take into account the fact that the InP bond in a Ge matrix should be under compressive strain, which upshifts the frequency. On the other hand, there is a weak peak at about the same frequency even in bulk Ge. This is a second-order Raman feature that has been reported previously.[25] Therefore, an alternative explanation for the 320 cm^{-1} peak is second-order Raman scattering involving mainly Ge-like modes, which for 364 nm excitation could become more resonant in the $(InP)_yGe_{5-2y}$ material due to changes in the electronic structure induced by alloying. Selective resonances of specific second-order Raman features have already been reported for Ge.[26]

The frequency shift of the main peak relative to bulk Ge can be rationalized in terms of a simple model that considers the main contributions to frequency shifts in alloy semiconductors.[22] For the Ge−Ge mode in $Ge_{1-z}Si_z$ alloys, this shift can be written as

$$\Delta\omega(z) = A\omega_0 z + B\omega_0(1 - a^{**})\frac{\Delta a_0(z)}{a_0} \quad (2)$$

where A and B are constants, ω_0 and a_0 are the bulk Ge Raman frequency and lattice parameter, respectively, a^{**} is the bond rigidity parameter defined by Cai and Thorpe,[27] and Δa_0 is the difference in lattice parameter between the alloy and bulk Ge. The first term in eq 2 is the so-called "mass" contribution, which mainly arises from the presence of atoms of different masses from those with large amplitudes in the Raman-active vibration. The second term is the "bond" contribution, which is caused by the bond distortions required to accommodate the alloy's average lattice parameter. The constants A and B have nearly universal values for all group IV alloy semiconductors,[28] and for the Ge−Ge mode the fit values are A = 0.11 and B = 2.60, very close to the theoretically expected values A = 0.1 and B = 3 based on a simple model.[28] When the alloy is grown as a thin film on a substrate, there is an additional contribution to the frequency shift due to the epitaxial strain, which in the case of (001)-oriented Ge is given by

$$\Delta\omega^{EPI} = -\gamma(2\varepsilon_{\parallel} + \varepsilon_{\perp})\omega_0 - \frac{2}{3}a_s\omega_0(\varepsilon_{\parallel} - \varepsilon_{\perp}) \quad (3)$$

Here $\varepsilon_{\parallel}$ and ε_{∞} are the components of the strain tensor parallel and perpendicular to the film surface, γ is the Grüneisen parameter, and a_s the shear phonon deformation parameter. For Ge, γ = 0.96 and a_s = 0.23.[29] If we assume the validity of eqs 2 and 3 for $(InP)_yGe_{5-2y}$ alloys, using $z = 2y/5$ and the parameters for the Ge−Ge mode in $Ge_{1-z}Si_z$, we predict a shift of −2.8 (−9.0) cm^{-1} for the $InPGe_{15}$ ($InPGe_5$) samples in Figure 9. This should be compared with the experimentally observed shifts of 0 cm^{-1} ($InPGe_{15}$) and −0.9 cm^{-1} ($InPGe_5$). It is therefore apparent that the Ge−Ge mode in $Ge_{1-z}Si_z$ alloys and the Ge−Ge mode in $(InP)_yGe_{5-2y}$ alloys cannot be described with a common model. It is instructive to speculate on the origin of this difference. To the extent that both systems follow Vegard's law to a very good approximation, it is hard to see why the terms in eqs 2 and 3 related to bond deformations (either in the relaxed alloy or induced by epitaxial strain) should be very different in the two systems. For the "mass" term in eq 2, on the other hand, the physics is quite different. Whereas in $Ge_{1-z}Si_z$ the fraction z of Si atoms is distributed at random, in $(InP)_yGe_{5-2y}$, the fraction $z = 2y/5$ of non-Ge atoms is not entirely at random because the In and P atoms appear in pairs. Therefore, for the same value of z, the probability that a Ge atom is bonded to another Ge atom is higher in $(InP)_yGe_{5-2y}$ than in $Ge_{1-z}Si_z$. Thus we should expect the mass term to be smaller in $(InP)_yGe_{5-2y}$, which is exactly what is observed. If we use A as an adjustable parameter, we find that the best fit is obtained for A = 0.016, a factor of 7 smaller than the $Ge_{1-z}Si_z$ value. The shifts predicted for this fit value are 0.53 cm^{-1} (−1.2) cm^{-1} for the $InPGe_{15}$ ($InPGe_5$) samples. The agreement with experiment is far from perfect but can be considered as acceptable in view of the partial cancelation of effects when eqs 2 and 3 are applied (which magnifies the errors) and to the compositional fluctuations observed in Figure 5, which may introduce additional shifts not included in our calculations. Further experimental and theoretical work will be needed to fully understand the vibrational properties of $(InP)_yGe_{5-2y}$ alloys, but the results so far appear consistent with the structural models consisting of bonded InP pairs in a Ge matrix.

Structural and Bonding Changes from Molecule to Solid. In our prior CVD synthesis of $Al(P_{1-x}N_x)_ySi_{5-2y}$ and $Al(As_{1-x}N_x)_ySi_{5-2y}$ alloys via reactions of Al atoms with $M(SiH_3)_3$ (M = N,P,As) molecules (or their mixtures), we envisioned[7−9] that the deliberate incorporation of molecular core structures into the solid products involves: (a) formation of intermediate "Al:$M(SiH_3)_3$" complexes, (b) desorption of molecular hydrogen, and finally, (c) some degree of structural adjustment of the molecular core to accommodate its new bonding environment within the covalent crystalline network. For the above Si-based systems we have already shown, using quantum chemistry and solid state simulations of the molecules and solids, that this "building-block" assembly process is both thermodynamically and chemically plausible.[9,10] Here we apply the same type of simulation approach to the Ge-based system, focusing for the first time on the analogous role of "In−P−Ge_3" cores delivered by In atom interactions with $P(GeH_3)_3$ molecules during the formation of the $(InP)_yGe_{5-2y}$ alloys,

dx.doi.org/10.1021/ja405726b | J. Am. Chem. Soc. 2013, 135, 12388−12399

the focal point of the present study. Specifically, we use density functional theory (DFT) in the local density approximation (LDA) for exchange correlation to simulate the ground-state energy and structure of both molecules and solids. Although more sophisticated DFT schemes might be warranted, we adopt the LDA here because its predictive ability is well-established and because it is implemented in both molecular and solid-state simulation packages, allowing meaningful structural trends to be compared within the same theoretical framework. In this regard, all molecular properties were generated by the Gaussian03 package[30] using 6-311++G-(3df,3pd) basis sets for all atoms, except indium, for which an effective core potential (ECP) was employed. To simulate the properties of solids, we applied the plane-wave basis VASP code,[31−33] which eliminates by-standing core electrons via ultrasoft pseudopotentials (ECPs). Electronic wave functions, potentials, and densities were expanded in a plane-wave basis up to an energy cutoff of 400 eV, and reciprocal space (k-point) integration grid density was optimized to ensure convergence of atomic forces, cell stress, and energy to levels below 0.01 eV/Å, 0.1 kBar, and 0.1 meV/atom, respectively.

The main results of our molecular simulations are summarized in Figure 10, which compares the structure and nucleophilic properties of the $P(GeH_3)_3$ and $P(SiH_3)_3$ precursors as well as the molecular core structure of the hypothetical $InH_3{-}P(GeH_3)_3$ with the corresponding structure of the "In−P−Ge_3" building block extracted from a typical ground-state crystal environment. In our growth experiments to date, the relative reactivity of the $P(SiH_3)_3$ and $P(GeH_3)_3$ precursors is in fact found to be quite similar, suggesting that the propensity of these molecules to donate bonding charge in the context of the Lewis acid−base coordination with group III atoms is also comparable. Here, we elucidate this tendency by mapping the total molecular electrostatic potential (ESP) onto an appropriate charge density contour to reveal electron-rich and electron-poor regions of the molecule associated with local nucleophilic and electrophilic character, respectively. The ESP maps for $P(GeH_3)_3$ and $P(SiH_3)_3$ molecules, shown in Figure 10a, corroborate the similar reactivity observed for these two molecules and indicate a slightly enhanced nucleophilic character (red shade) above the P atoms for the $P(GeH_3)_3$ compound. This similarity in chemical behavior likely originates from the very similar ground-state structures of $P(SiH_3)_3$ and $P(GeH_3)_3$ molecules which both consist of symmetrically canted silyl/germyl groups with downward-pointing apical hydrogen atoms, as shown in Figure 10b. In both cases, the calculated DFT−LDA bond lengths and angles are in reasonable agreement with available experimental values (in parentheses) obtained from gas electron diffraction studies.[34] As to the relative strength of acid−base interactions in the context of $P(GeH_3)_3$ "building blocks", we have previously estimated the heat of reaction for the related hypothetical Si-based $AlH_3{-}M(SiH_3)_3$ adducts to be in the range of −84 to −96 kJ/mol[10] by combining the enthalpy corrected electronic energies (at 298K) for the AlH_3 and $M(SiH_3)_3$ units and subtracting these from the corresponding values for the adducts. As shown in Figure 10c, the binding energy for the $InH_3{-}P(GeH_3)_3$ molecule is about −70 kJ/mol, which is only slightly weaker than the typical values for the Si-based analogues, indicating that the formation of "In:$P(GeH_3)_3$" intermediates and the subsequent incorporation of "In−P−Ge_3" cores into the solid is certainly plausible. The bottom panel of Figure 10c also summarizes the key bond lengths and

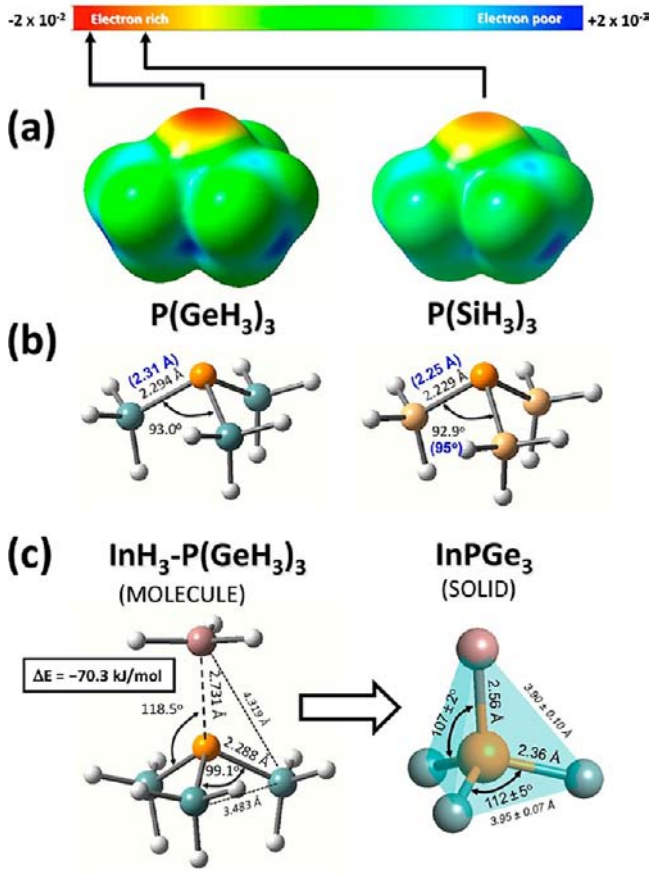

Figure 10. (a) Molecular electrostatic potentials (ESP) of the $P(GeH_3)_3$ and $P(SiH_3)_3$ molecules mapped onto their respective ρ = 0.0005 isodensity surfaces, showing a slightly enhanced nucleophilic character (red shade) above the P atoms in the $P(GeH_3)_3$ compound. (b) Equilibrium structures of $P(GeH_3)_3$ and $P(SiH_3)_3$, showing good agreement between calculated and experimental (in parentheses) bond lengths and angles. (c) Structure of the hypothetical $H_3In{-}P(GeH_3)_3$ adduct indicating slight P−Ge bond length contraction and ∠Ge−P−Ge bond angle opening in the "In−PGe_3" core (see text), resulting in a distorted tetrahedral structure. The corresponding "In−P−Ge3" units within the equilibrium crystal structure (bottom right) show that the molecular core is "regularized", exhibiting close to tetrahedral angles, edge lengths, and significantly reduced bond-length variance.

bond angles of the hypothetical $InH_3{-}P(GeH_3)_3$ compound. These are found to exhibit systematic changes relative to the parent $P(GeH_3)_3$ molecule very similar to those reported in our prior studies for the analogous $AlH_3{-}P(SiH_3)_3$ molecule in relation to its $P(SiH_3)_3$ parent. For example, here the dative bonding induces a contraction of <0.01 Å in the P−Ge bond lengths (∼2.29 Å) and ∼6° opening of the pyramidal (∠Ge−P−Ge ∼ 99°). Meanwhile, the In−P bond length and ∠Ge−P−In bond angle are calculated to be 2.73 Å and ∼119°, respectively, resulting in a significant departure from tetrahedral symmetry. This distortion leads to very dissimilar tetrahedral edge lengths, as indicated by dashed lines in the structure, corresponding to Ge−Ge (3.48 Å) and Ge−In (4.32 Å) distances.

To elucidate the nature and degree of "accommodation" required for the incorporation of the "In−P−Ge_3" building blocks into the solid, Figure 10c also shows a representative "In−P−Ge_3" tetrahedron extracted from the equilibrium crystalline structure (details of the solid state calculations are

dx.doi.org/10.1021/ja405726b | J. Am. Chem. Soc. 2013, 135, 12388−12399

presented below). As can be seen by comparing the structures in the left and right panels (molecule and solid, respectively), the core solid structure becomes substantially regularized when linked within its crystalline network. For instance, the In−P bond length in the adduct structure is shortened to 2.56 Å, very close to the corresponding LDA bond length of 2.52 Å in the binary InP alloy, while the P−Ge bond length dilates by 0.07 Å to a value of 2.36 Å. Furthermore, the internal bond angles approach the tetrahedral range such that ∠Ge−P−Ge ∼ 112.0 ± 0.5° and ∠Ge−P−In ∼ 107 ± 2°. Collectively, these bond length and bond angle adjustments lead to a dramatic regularization on the tetrahedral edge lengths which now span a range of 3.93 ± 0.10 Å, thereby facilitating the assembly of a tetrahedral framework. Similar comparisons for the $AlPSi_3$ and $AlAsSi_3$ systems[7,9,10] also predict more regularized tetrahedral structures, consistent with experimental observation based on XRD, XTEM, and Raman scattering analyses. On the basis of the deviations from perfect tetrahedral geometry of the "In−P−Ge_3" building-block structure in the crystalline habit predicted in Figure 10c, one might anticipate similar departures from the extended diamond-cubic form, as discussed below.

An intriguing aspect of $(InP)_yGe_{5-2y}$ alloy formation mechanism is that the concentration of In−P pairs can be systematically depleted relative to the limiting $InPGe_3$ composition via unimolecular $P(GeH_3)_3$ decomposition reactions at higher temperatures. These produce highly reactive germylene-like moieties which in turn enrich the Ge content of the solid product. The net result is the formation of a crystal consisting of In−P pairs completely isolated from one another, and in the limiting $InPGe_3$ case, the P atoms reside on a third-nearest neighbor sublattice in a manner that precludes the formation of energetically unfavorable In−In bonds. The lattice vectors of the primitive $InPGe_3$ cell containing two formula units are $\vec{a}_1 = a_0(-1/2,1,-1/2)$, $\vec{a}_2 = a_0(-1/2,1,1/2)$, and $\vec{a}_3 = a_0(-3/2,-1/2,0)$, where a_0 represents the crystallographic lattice constant of a conventional cubic diamond crystal and the Cartesian components are aligned with the conventional cubic (100), (010), and (001) directions in the parent diamond cubic lattice. For instance, the [001] projection is obtained from $\vec{a}_2 - \vec{a}_1 = a_0(0,0,1)$. The In, P, and Ge atoms are initially placed on a perfect diamond lattice using fractional coordinates provided in ref 9. Structural optimization then yields a static lattice ground-state structure possessing $C1c1$ symmetry with cell parameters $a = b = 6.971$ Å, $c = 8.932$ Å, $\alpha = \beta = 130°$, and $\gamma = 48.73°$ and atomic positions In(0.015,0.791,0.099), P(0.548,0.850,0.789), Ge(0.600,0.417,0.507), Ge(0.411,0.178,0.690), and Ge(0.260, 0.951,0.907). This unit cell possesses a nearly cubic symmetry, as can be seen from the (110) projection shown in Figure 11, which also illustrates the slight departures from perfect diamond cubic symmetry in which the In, P, and Ge atoms are not precisely aligned. Although the foregoing ground-state results were obtained using the primitive 10-atom setting, a more general 20-atom representation containing four $InPGe_3$ units can be used to identify higher energy metastable configurations containing various alternative "In−P" dimer orientations devoid of In−In nearest-neighbor bonds. Using the notation $\{V_1,V_1',V_1'',V_1'''\}$ established in our prior work,[9] the ground-state $InPGe_3$ structure described above corresponds to {1111}, while configurations {1432} and {1214} with energies +22.6 and +24.0 meV/atom above the ground-state (respectively) are found to possess slightly expanded molar volumes of +0.16 and +0.33%. Accordingly, the existence of slightly metastable configurations containing orientationally disordered "In−P" dimers may also be thermodynamically plausible and can lead to composition-independent molar volume fluctuations.

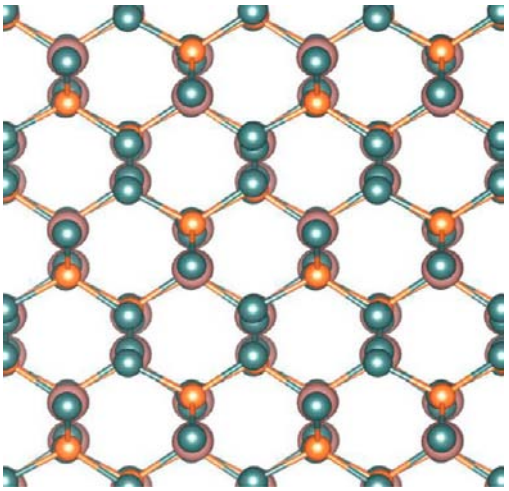

Figure 11. View of the optimized $InPGe_3$ crystal structure along the crystallographic [110] direction indicating slight deviations from perfect diamond symmetry as evidenced by misalignment of the "dumbbells" pairs (In, P, and Ge atoms are shown as pink, orange, and green spheres, respectively).

To further elucidate the experimental studies over the broader composition range of the synthesized alloys ($InPGe_{15}$ to $InPGe_{4.6}$), we next constructed a series of supercells containing up to 20 atoms and substituted the requisite number of In−P pairs by Ge atoms to yield systems with composition $InPGe_{18}$ and $InPGe_8$. To eliminate scaling artifacts, we also used the same supercell structures to calculate the corresponding ground-state properties of Ge (cubic diamond) and binary InP (zincblende) end members. Our main simulation results for the solid state $(InP)_yGe_{5-2y}$ systems are summarized in Table 1 and Figure 12, where they are compared with the corresponding experimental systems for which relaxed lattice constants have been determined from XRD measurements. The data listed in Table 1 includes the static lattice ground-state energy per atom (E_0) showing the expected trend of decreasing binding energy from Ge to InP.

Table 1. Summary of LDA Calculations for $(InP)_yGe_{5-2y}$ Alloys Including Static Lattice Energies Relative to the Ge and InP End Members, Equivalent Cubic Lattice Parameters $\langle a_0 \rangle$, Corrected LDA Values (See Text), and Experimental a_0 Values Determined by XRD

system	E_0/atom (eV)	ΔE/atom (meV)	$\langle a_0 \rangle_{LDA}$ (Å)	$\langle a_0 \rangle_{LDA} + \Delta a$ (Å)	a_0^{EXP} (Å)
Ge	−5.1997	0	5.625	5.658	5.658
$InPGe_{18}$	−5.1329	33	5.646	5.680	
$InPGe_{15}$					5.673
$InPGe_{8.9}$					5.684
$InPGe_8$	−5.0769	56	5.662	5.697	
$InPGe_{7.5}$					5.690
$InPGe_{6.3}$					5.696
$InPGe_{5.2}$					5.703
$InPGe_5$					5.701
$InPGe_{4.6}$					5.699
$InPGe_3$	−4.9776	88	5.698	5.734	
InP	−4.8638	0	5.828	5.869	5.869

dx.doi.org/10.1021/ja405726b | J. Am. Chem. Soc. 2013, 135, 12388−12399

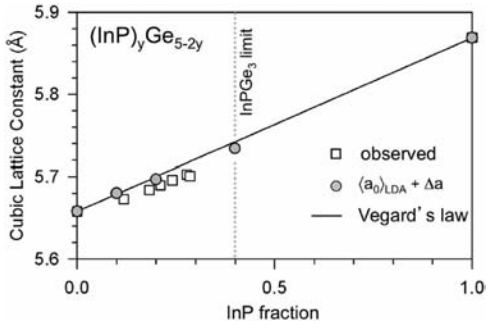

Figure 12. Plot of the corrected LDA and observed lattice constants as a function of InP content showing a close correspondence with Vegard's law (solid line). The vertical dotted line indicates the maximum 40% InP composition possible via incorporation of intact "In−P−Ge_3" units.

The energy ΔE is an approximation to the formation enthalpy of a given compound relative to Ge and InP and is obtained as the difference between the $(InP)_yGe_{5-2y}$ alloy energy and that of the corresponding stoichiometric sum of InP and Ge end-members. The positive values for ΔE indicates that all systems are metastable relative to the binary InP alloy and Ge. The effective cubic LDA lattice parameters, listed as $\langle a_0 \rangle$ in the table, were obtained from the diamond-like optimized structures by $(8\Omega_0)^{1/3}$, where Ω_0 is the volume per atom of a given system. These lattice constants were then corrected to account for the typical underestimate obtained from the LDA by including a composition-dependent linear correction Δa varying from 0.6 to 0.7% of $\langle a_0 \rangle$ in going from Ge to InP. This allows a straightforward comparison of experimental and theoretical trends with respect to Vegard's law, as shown by the plot in Figure 12, where the agreement between the observed and predicted data is seen to be very good. We note that a slight negative bowing behavior away from ideal Vegard behavior is both observed and predicted on the basis our LDA calculations.

Finally, we briefly investigated the electronic structure of the fully stoichiometric $InPGe_3$ alloy within the framework of the local density approximation (LDA) for exchange and correlation. Routine band structure calculations of the InP and Ge end-members using this level of theory and primitive cells containing only two atoms (zincblende and diamond structures, respectively), yield a direct gap of 0.56 eV for InP and a vanishing fundamental band gap in Ge. The severe underestimation of band gaps, and the closure of the fundeamental gap in Ge, are well-known failures of the LDA. Nevertheless, the compositional trends of the critical points corresponding to key transitions between the valence and conduction band (energy differences) in alloy systems are often quantitative. Here we apply this approach, with its inherent limitations, to the calculation of band structure in InP, $InPGe_3$, and Ge by adopting a common 10-atom representation for all three systems. This allows a direct comparison of the critical point energies. Use of lattice vectors whose Cartesian components are aligned with conventional diamond lattice plane simplifies the interpretation of the band structure as shown in Figure 13, which illustrates the composition

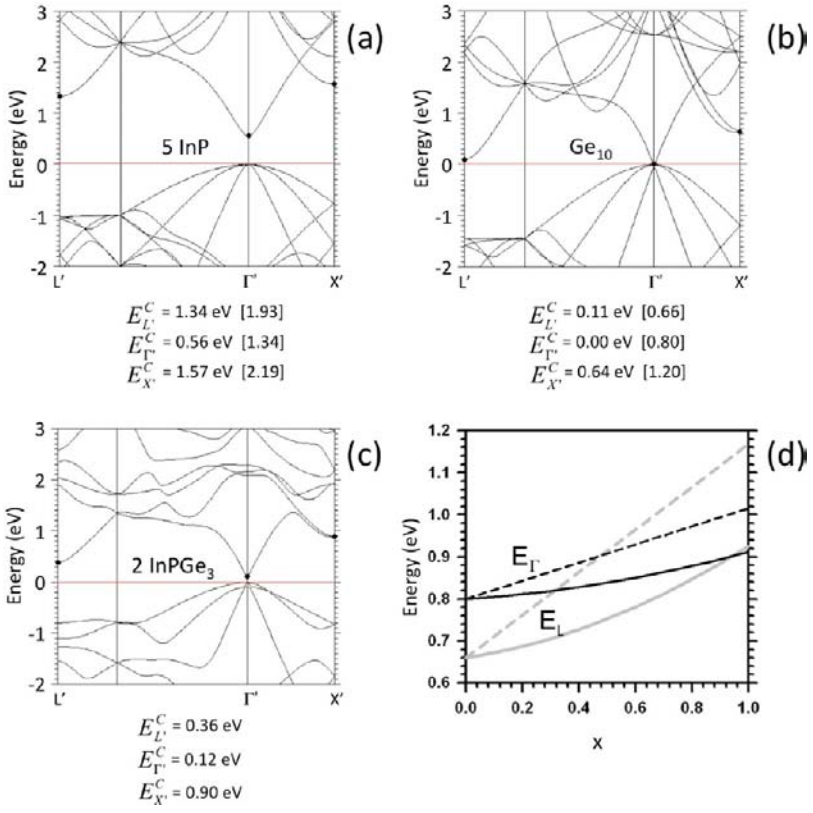

Figure 13. (a−c) LDA band structure plots of InP, $InPGe_3$, and Ge, respectively, using a common 10-atom representation (see text). Critical points are indicated by solid dots and the corresponding numerical values are listed below each panel (experimental values in square brackets) and indicate a marginally direct gap in $InPGe_3$ at this level of theory. (d) Composition dependence of the Γ and L point energy gaps obtained by linearly interpolating between experimental values (dashed lines) and by including a bowing correction deduced from the LDA band structure (solid lines).

dx.doi.org/10.1021/ja405726b | J. Am. Chem. Soc. 2013, 135, 12388−12399

dependence of the energy bands in the salient portion of the gap region. The *k*-points L′, Γ′, and X′ in the 10-atom representation correspond to the conventional L, Γ, and X directions in the FCC lattice (additional valence and conduction band states at L′, Γ′, and X′ are due to Brillouin zone folding). The calculated values of the critical point energies in the $InPGe_3$ alloy are slightly lower than the Vegard average, indicating negative compositional bowing. From the LDA critical point energies contained in the figure we obtain bowing parameters $b_L = -1.008$ eV, $b_\Gamma = -0.433$ eV, and $b_X = -0.467$ eV. As discussed earlier in connection with our PL measurements on $(InP)_xGe_{5-2x}$ alloys, a linear compositional interpolation between the (InP and Ge) end members predicts an indirect-to-direct crossover near $x \sim 0.5$ and a corresponding direct gap of ∼0.9 eV. However, incorporation of the calculated LDA-derived bowing parameters shifts this crossover to $x \sim 0.95$, leading to a direct gap of ∼0.91 eV in $InPGe_3$ (we note that the use of $E_L[InP] = 1.88$ eV in place of the value 1.93 eV listed in Figure 13 lead to a slight shift of the indirect−direct crossover to $x \sim 1$). In future work, we will re-examine the band structure in this class of alloys with a focus on indirect−direct behavior using more quantitative methods such as the GW approximation.

CONCLUSIONS

In this study, we demonstrated, for the first time, the synthesis of a class of monocrystalline $(InP)_yGe_{5-2y}$ alloys on Ge/Si(100), with InP content between 10 and 30% using an approach previously developed to successfully fabricate analogous $Si_{5-2y}(AlX)_y$ {X = N,P,As} semiconductors directly on Si(100). Structural characterization of the $(InP)_yGe_{5-2y}$ materials indicate that they possess composition-dependent lattice constants, while PL studies indicate a concomitant variation in band gap behavior and possible direct gap values below that of Ge (0.80 eV) in the near IR. Density functional theory simulations at both the molecular and solid-state level were used to elucidate the assembly pathway, from precursor interactions, to formation of intermediate "building-block" structures, to the solid product, and indicate that the overall process is thermodynamically favorable. The observed dependence of the $(InP)_yGe_{5-2y}$ lattice constants on InP content is closely reproduced by our first principles simulations, and the corresponding Raman spectra are consistent with the "In−P−Ge_3" building-block interpretation of the crystal structure. Collectively, our work provides further compelling evidence for the generality of a "building-block" approach to the assembly of robust, covalent crystalline solids, opening the door to a vast range of hitherto inaccessible III−V−IV solid compositions with potentially useful technological applications.

AUTHOR INFORMATION

Corresponding Author

chizmesh@asu.edu

Notes

The authors declare no competing financial interest.

ACKNOWLEDGMENTS

This work was supported by the U.S. Air Force under contract AFOSR FA9550-12-1-0208 and by the U.S. National Science Foundation under grant no. DMR-0907600. We thank Toshihiro Aoki for his assistance with TEM characterization.

REFERENCES

(1) Noreika, A. J.; Francombe, M. H. *J. Appl. Phys.* **1974**, *45*, 3690.
(2) Cadien, K. C.; Eltoukhy, A. H.; Greene, J. E. *Appl. Phys. Lett.* **1981**, *38*, 773.
(3) Banerjee, I.; Chung, D. W.; Kroemer, H. *Appl. Phys. Lett.* **1985**, *46*, 494.
(4) Norman, A. G.; Olson, J. M.; Geisz, J. F.; Moutinho, H. R.; Mason, A.; Al-Jassim, M. M.; Vernon, S. M. *Appl. Phys. Lett.* **1999**, *74*, 1382.
(5) Newman, K.; Dow, J. *Phys. Rev. B* **1983**, *27*, 7495.
(6) Giorgi, G.; Schilfgaarde, M.; Korkin, A.; Yamashita, K. *Nanoscale Res. Lett.* **2010**, *5*, 469.
(7) Watkins, T.; Chizmeshya, A. V.; Jiang, L.; Smith, D. J.; Beeler, R. T.; Grzybowski, G.; Poweleit, C. D.; Menendez, J.; Kouvetakis, J. *J. Am. Chem. Soc.* **2011**, *133* (40), 16212.
(8) Watkins, T.; Jiang, L.; Xu, C.; Chizmeshya, A. V. G.; Smith, D. J.; Menéndez, J.; Kouvetakis, J. *Appl. Phys. Lett.* **2012**, *100* (2), 022101.
(9) Grzybowski, G.; Watkins, T.; Beeler, R. T.; Jiang, L.; Smith, D. J.; Chizmeshya, A. V. G.; Kouvetakis, J.; Menéndez, J. *Chem. Mater.* **2012**, *24* (12), 2347.
(10) Kouvetakis, J.; Chizmeshya, A. V. G.; Jiang, L.; Watkins, T.; Grzybowski, G.; Beeler, R. T.; Poweleit, C.; Menéndez, J. *Chem. Mater.* **2012**, *24* (16), 3219.
(11) Jiang, L.; Sims, P. E.; Grzybowski, G.; Beeler, R. T.; Chizmeshya, A. V. G.; Smith, D. J.; Kouvetakis, J.; Menéndez, J. *Phys. Rev. B* **2013**, *88*, 045208.
(12) Kehoe, A. B.; Temple, D. J.; Watson, G. W.; Scanlon, D. O. *Phys. Chem. Chem. Phys.*, **2013**, DOI: 10.1039/C3CP52482E.
(13) Carenco, S.; Portehault, D.; Boissie, C.; Mezailles, N.; , and Sanchez, C. *Chem. Rev.* **2013**,DOI: 10.1021/cr400020d.
(14) Kouvetakis, J.; Mathews, J.; Roucka, R.; Chizmeshya, A. V. G.; Tolle, J.; Menéndez, J. *IEEE Photonics J.* **2010**, *2* (6), 924−941.
(15) Sohn, H.; Weber, E. R.; Nozaki, S.; Takahashi, K. *Appl. Phys. Lett.* **1995**, *67*, 1104.
(16) Lautenschlager, P.; Garriga, M.; Cardona, M. *Phys. Rev. B* **1987**, *36*, 4813.
(17) Yang, J. H.; Zhai, Y.; Liu, H.; Xiang, H.; Gong, X.; Wei, S. H. *J. Am. Chem. Soc.* **2012**, *134* (30), 12653.
(18) Kolyubakin, A. I.; Osp'yan, Y. A.; Shevchenko, S. A.; Shteinman, É. A. *Sov. Phys. Solid State* **1984**, *26* (3), 407.
(19) Vurgaftman, I.; Meyer, J. R.; Ram-Mohan, L. R. *J. Appl. Phys.* **2001**, *89*, 5815.
(20) Kim, J.; Fischetti, M. V. *J. Appl. Phys.* **2010**, *108*, 013710.
(21) D'Costa, V. R.; Cook, C. S.; Birdwell, A. G.; Littler, C. L.; Canonico, M.; Zollner, S.; Kouvetakis, J.; Menendez, J. *Phys. Rev. B* **2006**, *73*, 125207.
(22) Fujii, M.; Hayashi, S.; Yamamoto, K. *Appl. Phys. Lett.* **1990**, *57* (25), 2692.
(23) Mooradian, A.; Wright, G. B. *Solid State Commun.* **1966**, *4* (9), 431.
(24) Fritsch, J.; Pavone, P.; Schröder, U. *Phys. Rev. B* **1995**, *52* (15), 11326.
(25) Weinstein, B. A.; Cardona, M. *Phys. Rev. B* **1973**, *7* (6), 2545.
(26) Renucci, M. A.; Renucci, J. B.; Zeyher, R.; Cardona, M. *Phys. Rev. B* **1974**, *10* (10), 4309.
(27) Cai, Y.; Thorpe, M. F. *Phys. Rev. B* **1992**, *46* (24), 15872.
(28) D'Costa, V. R.; Tolle, J.; Poweleit, C. D.; Kouvetakis, J.; Menéndez, J. *Phys. Rev. B* **2007**, *76* (3), 035211.
(29) Singh, R.; Poweleit, C. D.; Dailey, E.; Drucker, J.; Menéndez, J. *Semicond. Sci. Technol.* **2012**, *27* (8), 085008.
(30) Frisch, M. J.; Trucks, G. W.; Schlegel, H. B.; Scuseria, G. E.; Robb, M. A.; Cheeseman, J. R.; Montgomery, J. A., Jr.; Vreven, T.; Kudin, K. N.; Burant, J. C.; Millam, J. M.; Iyengar, S. S.; Tomasi, J.; Barone, V.; Mennucci, B.; Cossi, M.; Scalmani, G.; Rega, N.; Petersson, G. A.; Nakatsuji, H.; Hada, M.; Ehara, M.; Toyota, K.; Fukuda, R.; Hasegawa, J.; Ishida, M.; Nakajima, T.; Honda, Y.; Kitao, O.; Nakai, H.; Klene, M.; Li, X.; Knox, J. E.; Hratchian, H. P.; Cross, J. B.; Bakken, V.; Adamo, C.; Jaramillo, J.; Gomperts, R.; Stratmann, R. E.; Yazyev, O.; Austin, A. J.; Cammi, R.; Pomelli, C.; Ochterski, J. W.;

Ayala, P. Y.; Morokuma, K.; Voth, G. A.; Salvador, P.; Dannenberg, J. J.; Zakrzewski, V. G.; Dapprich, S.; Daniels, A. D.; Strain, M. C.; Farkas, O.; Malick, D. K.; Rabuck, A. D.; Raghavachari, K.; Foresman, J. B.; Ortiz, J. V.; Cui, Q.; Baboul, A. G.; Clifford, S.; Cioslowski, J.; Stefanov, B. B.; Liu, G.; Liashenko, A.; Piskorz, P.; Komaromi, I.; Martin, R. L.; Fox, D. J.; Keith, T.; M. A. Al-Laham, Peng, C. Y.; Nanayakkara, A.; Challacombe, M.; Gill, P. M. W.; Johnson, B.; Chen, W.; Wong, M. W.; Gonzalez, C.; Pople, J. A. *Gaussian 03*, Revision C.02; Gaussian, Inc.: Wallingford CT 2004.

(31) Kresse, G.; Hafner, J. *Phys. Rev. B* **1993**, *47* (1), 558.

(32) Kresse, G.; Furthmüller, J. *Comput. Mater. Sci.* **1996**, *6* (1), 15.

(33) Kresse, G.; Furthmüller, J. *Phys. Rev. B* **1996**, *54* (16), 11169.

(34) Rankin, D. W. H; Robiette, A. G.; Sheldrick, G. M.; Beagley, B.; Hewitt, T. G. *J. Inorg. Nucl. Chem.* **1969**, *31*, 2351.